ndt

MDPI

Article

Monitoring the Calibration Status of a Universal Testing Machine Through the Implementation of Acoustic Methods: Development of Equipment and a Suitable Interface

Sharath P. Subadra [1,2,*], Roy Skaria [1,2], Andrea Hasselmann [1,2], Eduard Mayer [1,2] and Shahram Sheikhi [1,2]

[1] Institute of Materials Science and Joining Technology, University of Applied Science Hamburg, Berliner Tor 13, D-20099 Hamburg, Germany; shahram.sheikhi@haw-hamburg.de (S.S.)
[2] Forschungs-und Transferzentrum 3i, University of Applied Science Hamburg, Berliner Tor 13, D-20099 Hamburg, Germany
* Correspondence: sharath.peethambaransubadra@haw-hamburg.de

Abstract: The calibration of a universal testing machine (UTM) verifies the accuracy of the system instruments responsible for obtaining force and displacement measurements. This process involves comparing the instrument to equipment that has already been calibrated to a known traceable standard. The limit of accuracy is then certified and the traceability of the measurements is determined. There are several internationally recognized standards that are used to calibrate the cross-head speed and displacement (ASTM E2658 and E2309, respectively), strain and load rate (ASTM E2309), measurement of tension, compression (ASTM E4) and dynamic force (ASTM E467). The current study aims to monitor the calibration status of UTMs through the implementation of acoustic methods. A methodology is developed whereby a reference sample is initially identified with suitable material properties, enabling it to be used continuously. The sample is used simultaneously with acoustic instruments to check its natural frequencies, which enables the monitoring of the UTM calibration status. An algorithm is developed that enables the user to interact with the system, thus forming an interface and helping the user to check the calibration status of the equipment. The entire system is validated to check if the equipment and the inbuilt algorithm can predict the calibration status of the machine. It was found that the geometric constraints imposed on the sample influence the output from the algorithm, and hence correct values should be fed to the system. Our sample never lost its elastic characteristics through continuous use, demonstrating that it can be used to continuously monitor the machine's status.

Keywords: non-destructive testing; universal testing machine; acoustics; calibration; AI; prediction; monitoring

Academic Editor: Fabio Tosti

Received: 14 October 2024
Revised: 12 December 2024
Accepted: 15 December 2024
Published: 2 January 2025

Citation: Subadra, S.P.; Skaria, R.; Hasselmann, A.; Mayer, E.; Sheikhi, S. Monitoring the Calibration Status of a Universal Testing Machine Through the Implementation of Acoustic Methods: Development of Equipment and a Suitable Interface. *NDT* **2025**, *3*, 2. https://doi.org/10.3390/ndt3010002

1. Introduction

A uniaxial tensile test is the primary method adopted to control and certify all metallic materials. In total, 80 million tons per annum of various ferrous and non-ferrous alloys are sold throughout Europe, with an estimated value of over EUR 50,000 million [1]. Carrying out reliable tensile testing on UTMs is crucial in the design of many critical safety components, such as in power plants, or in nuclear and aerospace applications, for which any inaccuracy can be catastrophic.

The calibration of UTMs involves the use of reference samples that are certified and that adhere to respective standards. The material properties of these reference samples are

known, and any deviation found while attempting calibration with these samples denotes a loss of calibration in the UTM. Therefore, a certified reference sample provides proof of the stability of the UTMs before any decision on calibration needs to be made. By referring to the reference sample's parameters, the suitability of the established parameters in the testing software can also be checked. Reference samples can also be used to determine the compliance of the measurement uncertainty to established standards, which is of interest for customers [2]. Therefore, when using reference samples to monitor such deviations, the samples are irreversibly destroyed in the process of carrying out the comparison between its stated material properties and those derived from the machine while being tested, thereby increasing overall costs. A major issue of normal calibration is the significant intervals involved and ISO 9001 [3] necessitates calibration of all measuring devices annually. However, these intervals can be longer depending on several factors and significant deviations from the calibrated state can occur within these intervals, in turn affecting the accuracy of the mechanical properties that are determined.

Young's modulus (E) is an intrinsic material property, and a key parameter in engineering design and material development. The current mechanical test methods used to ascertain this value are still not well established. Several tensile testing standards, like EN10002-1 [4], ASTM E8 [5] and ISO 6892 [6], focus on measuring the full stress–strain curve until the point of failure, with the elastic region forming a small part of the overall curve where E is measured. Apart from being a very important engineering term, vital for design studies and used in finite element modelling to achieve reliable fits, etc., E values are also necessary for obtaining reliable values for proof stress. In addition to this, E values can also be used to monitor or to check the UTM calibration status.

E is defined as the stress/strain ratio under elastic loading. Traditionally, it is determined from a line drawn through the linear portion of the stress–strain curve, but newer machines from Instron (Illinois Tool Work Inc., Glenview, IL, USA), Zwick-Roell GmbH & Co., Ulm, Germany and Galdabini S.p.A., Cardano Al Campo, Italy in combination with newer data acquisition systems provide better curve fittings for the calculation of E. Tensile testing standards generally provide little guidance on how to determine the E value of the elastic zone. Table 1 provides an overview of the information within this context.

Table 1. Comparisons between ISO 6892 and ASMT E8 [5,6].

	ISO 6892	ASTM E8
Scope	Mechanical properties at room temperature. No explicit method to determine E, though ISO 6892 [6] elaborates on a range that can be used to determine the slope. Linear regression of the linear range is as follows: Lower limit: ~10% of $R_{p0.2}$ Upper limit: ~50% of $R_{p0.2}$	
Test conditions	Hysteresis tests can be employed to measure the modulus and the slope. Preloads permitted, but the value must be noted.	
Speed of testing	Different speeds recommended along the entire stress–strain curve.	
Extensometer	For determination of proof strength, the extensometer can be used in accordance with ISO 9513 (Class 1). For other properties, Class 2 based on ISO 9513 is used [7].	Class B-2 for R_{eL}, R_{eH} and A_t. Average extensometry recommended for R_{eL}, R_{eH}.
Repeat measurements	Not applicable	
Uncertainty	There is a detailed measurement routine to determine uncertainties in measured properties such as R_{eH}, R_{eL}, etc., but not for E.	Some advice regarding precision statistics, but no uncertainty calculations.

$R_{p0.2}$ —proof strength at 0.2% offset; R_{eL}—lower yield strength; R_{eH}—upper yield strength; A_t —total Elongation.

In this study, we adhere to established guidelines for determining E, which is computed within the elastic region defined by ranges corresponding to lower and upper limits [8]. Defining the limits shall be shown in the result section, but the obtained E is influenced by various uncertainties associated with the measuring instrument. The most widely recognised sources of uncertainties are from dimensional measurement devices, gauge determination systems, type of extensometer, alignment systems, stiffness of testing machines, accuracy in force measurement, precision of extensometers, rates of stress and strain, systems of data acquisition, the rate of data acquisition and software used for testing [9]. The following question naturally arises: how can E be used to monitor UTM calibration status if E is itself subject to so many uncertainties? The answer is that its value itself depends on these uncertain variables, and ultimately provides insight into the condition of the instruments measuring these variables. The degree of uncertainty in these variables can be estimated according to established standards. A certificate is provided after the UTM is calibrated, and it includes the uncertainties. The E value recorded from this type of equipment will ultimately differ from the value taken on the calibration day, and according to standard regulations, this deviation should not exceed 5%. This variation inE arises from the equipment's possible loss of calibration over time, which can be measured and will be discussed in the following section [9].

Apart from the above-discussed methods to estimate E, which are termed direct methods, several indirect methods (also termed dynamic measurement methods) such as non-destructive methods that use sound waves can also be employed. There are four primary sources of uncertainties, which relate to the measurements of the test piece, the apparatus, the environment and the operator/procedure. Consequently, these methods are much more adaptable to industrial use and are simpler, cheaper and quicker [10]. It has been observed that dynamic measurements for determining E are significantly more precise, with an error margin of about $\pm 1\%$ [10]. These methods entail applying an impulse to the sample that causes it to vibrate, recorded by a microphone/accelerometer, non-contact vibrometer, or piezo crystal. The measurement device's output, represented as a time-domain signal, is transformed into the frequency domain using fast Fourier transforms (FFTs), revealing the frequency peaks in a spectrum. The relevant frequency peaks are identified, and subsequently plugged into equations derived based on Eulers–Bernoulli theory to obtain the elastic properties including E [10–17].

In this article, the authors detail a method for assessing the calibration status of UTMs by integrating two recognized testing methods, namely tension tests and acoustic emission tests, using a reference sample that can be applied non-destructively. The tension tests are conducted in the elastic region of the reference sample, thus utilizing E to monitor the machine condition. Two materials, specifically EN AW-6060 (AlMgAi0,5), commonly referred to as 3.3206, categorized under the group of hardenable aluminium–magnesium–silicon alloys (referred to as AL6060 in this paper), and high-strength low-alloy fine-grain steel commercially known asALFORM700M® (referred to as M700 in this paper), are utilized due to their appropriateness as a non-destructive reference sample. The E values derived from acoustics are compared with those obtained from tension tests, by employing a software application developed in-house and integrated into the machine. A suitable graphical user interface that provides visual interface for users with the software application is implemented and will be discussed in this paper. The software application allows users to regularly verify the calibration status of machine, thereby ensuring adherence to quality norms associated with materials. Thus, the integration of two aspects, i.e., creation of a non-destructive reference sample and a software application to monitor UTM calibration status, has not yet been realized to the author's knowledge.

The paper is organized as follows: first, after this section, the paper elaborates on the mathematical approach to identify the uncertainties associated with measuring E. Next, the theoretical considerations with respect to uncertainty measurement and acoustics shall be presented, followed by a discussion on the experimental methodology. The results and discussions are detailed in the subsequent sections, followed by the conclusions.

2. Theoretical Considerations

2.1. Uncertainty Measurements

Based on [18], sources of uncertainties are grouped into the following four categories:

(a) Those related to test piece measurements;
(b) Those associated with testing apparatus;
(c) Those due to the environment;
(d) Those due to operator procedures.

The first two are addressed based on the equations elaborated in this section. According to Gabauer [18], environmental uncertainties stem from temperature and moisture levels. Consequently, precautions are taken so that the reference samples utilized in this study are not exposed to extreme variations arising from temperature and moisture. The factors related to operator procedures such as, zeroing, stress rate, strain rate, and digitizing are addressed by conducting tests under a protocol that considers these factors. Moreover, adhering to the testing procedure in ISO 6892, we are able to address these issues effectively.

Obtaining accurate values of the elastic modulus on UTMs depends on many factors, which can be attributable to the first two points highlighted above. Based on Hooke's law, the elastic modulus can be expressed as follows:

$$E = \frac{\sigma}{\varepsilon} = \frac{F \cdot l_0}{A_0 \cdot \Delta l} \tag{1}$$

where E is the elastic modulus, σ is the stress, ε is the strain, F is the tensile force applied during the test, l_0 is the initial gauge length of the test specimen, A_0 is the initial cross-sectional area of the test specimen and Δl is the change in the gauge length. From Equation (1), it is obvious that E is dependent on four parameters, as shown below:

$$E = f(F, l_0, A_0, \Delta l) \tag{2}$$

The functions highlighted in Equation (2) are linked to the categories (a) and (b) that were explained earlier. Therefore, the uncertainties are a function of each of the measured quantities in Equation (2), and these add up to the final measured E. The measured uncertainty can be expressed as follows:

$$u(y) = \sqrt{\left(u(x_1)^2 + u(x_2)^2 + \ldots + u(x_n)^2\right)} \tag{3}$$

where $u(x_1)$ is the uncertainty in the parameter x_1. Each of the factors from Equation (2) can be assigned to the parameters in Equation (3). Therefore, Equation (3) can be re-written as follows:

$$u(y) = \sqrt{\left(u(F)^2 + u(l_0)^2 + u(A_0)^2 + u(\Delta l)^2\right)} \tag{4}$$

Further elaborating on each of the uncertainty in the parameters (i.e., $u(F), u(l_0), u(A_0), u(\Delta l)$), Equation (4) can be expanded as follows:

$$u(y) = \sqrt{\left(\frac{1}{F}\right)^2 . W_F^2 + \left(\frac{1}{l_0}\right)^2 . W_{l_0}^2 + \left(\frac{-1}{A_0}\right)^2 . W_{A_0}^2 + \left(\frac{-1}{\Delta l}\right)^2 . W_{\Delta l}^2} \tag{5}$$

In Equation (5), W_F is the uncertainty of the load cell, which can be obtained from the calibration certificate. W_{l_0} is the influence of the uncertainty stemming from the measurement of the initial length l_0 using a calliper. W_{A_0} is the uncertainty stemming from the measurement of the cross-sectional area of the sample. Lastly, W_{Δ_l} is the uncertainty measurement of elongation in the elastic region by the extensometer and this information can also be obtained from the calibration certificate. Thus, Equation (5) defines the limits of the uncertainties measured in relation to the reference value E calculated from Equation (1). This implies that the measured uncertainty from experiments shall be within the intervals defined by Equation (5), and the experimentally determined values of the elastic modulus should be within the limits defined by the following equation:

$$E_{exp} = E \pm u(y) \tag{6}$$

Thus, in our study, we measure and quantify all the uncertainties linked to the extensometer, load and measurement of samples. The quantified values are inserted into Equation (6) along with the E obtained from the experiments. The uncertainty corresponds to each measured E, and if the total E exceeds 5% of the original value, it is interpreted as a deviation in calibration status [18–24].

2.2. E Measurement by Acoustic Means

Determination of E of a prismatic beam featuring an asymmetric cross-section around a single axis relies on three vibration modes: out-of-plane, in-plane bending modes and longitudinal vibration modes. The risk of combined modes occurring when out-of-plane modes are activated is very low. The bending vibration of beams that obey the Eulers–Bernoulli theory is a better choice to ascertain the modes and the respective frequencies. The derivation of the respective equations is outside the scope of this paper since they are widely available in the literature [25]. The equations being considered for this paper refer to a beam that is a cantilever type (boundary conditions) and are presented as Equation (7):

$$\omega_n = C_n \sqrt{\frac{EI}{\rho A L^4}} \tag{7}$$

where C_n takes into account different boundary conditions that are presented in Table 2. The other terms are either geometry-related or other material properties of the structure, i.e., I is the moment of inertia of the cross-section, h is the thickness, ρ is the density, L is the length of the structure and f is the natural frequency. With respect to Equation (7), the width of the sample is different along the central part of the sample. To take into account this variation, the moment of inertia is divided into three parts along with the area as seen in Equation (8). Further expansion leads to the width (b) being cancelled out as seen in Equation (9). The final equation with E is shown in Equation (10).

$$\omega_n = C_n \sqrt{\frac{E(I_1 + I_2 + I_3)}{\rho(A_1 + A_2 + A_3)L^4}} \tag{8}$$

$$\omega_n = C_n \sqrt{\frac{E\frac{h^3}{12}(b_1 + b_2 + b_3)}{\rho h(b_1 + b_2 + b_3)L^4}} \approx C_n \sqrt{\frac{Eh^2}{12\rho L^4}} \tag{9}$$

$$E = \frac{\rho L^4}{h^2}\left(\frac{48\pi^2 f^2}{C_n^2}\right) \tag{10}$$

As shown in the above equation, the boundary conditions defined by C_n need to be examined. Since a simply supported structure is not considered in this study, it is omitted.

The fixed–fixed and fixed–free conditions are examined with respect to the reference sample and an appropriate boundary condition is selected, which is subsequently used for this study [25].

Table 2. C_n for different boundary conditions and modes.

Modes (n)	Boundary Conditions		
	Simply Supported	Fixed–Fixed	Fixed–Free
1	π^2	22.3733	3.5160
2	$4\pi^2$	61.6728	22.0345
3	$9\pi^2$	120.9034	61.6972
4	$16\pi^2$	199.8594	120.0902
5	$25\pi^2$	298.5555	199.8600

3. Methods

3.1. Reference Sample

This study focuses on creating a non-destructive reference sample, and two materials were considered for this purpose. As stated in Section 1, AL6060 and M700 were selected as potential materials for the reference sample. Several factors back the choice, but the primary consideration is the fatigue threshold, which is significantly influenced by the grain size and its distribution, the slip character of dislocations, etc. [26,27]. The latter is an important aspect affecting the fatigue threshold, which is determined by the stacking fault energy (SFE) and the coherence level of precipitates. The coherent precipitates enhance the more planar slip nature by aiding the reversibility of dislocation gliding at the crack tip [26,28]. Fewer dislocations are observed in microplastic processes at the crack tip, when compared to incoherent precipitates in some materials [26,29]. Thus, roughness-induced crack closure and crack deflection are predominant, and hence higher fatigue thresholds are achieved [28]. AL6060 and M700 are both precipitation-hardened; where in the latter, it is precipitation hardened by addition of Ti, Nb and V and in the former, the precipitation sequence is as follows:

Mg- and Si-atom clusters → co-clusters of Mg and Si → GP-I zones (coherent) → GP-II zones (β″-needles, coherent along the needle axis) → β′ rods (semi-coherent) → β-Mg_2Si plates (incoherent) [30,31].

The sample dimensions are machined as per DIN 50125 [32], and the dimensions are as shown in Figure 1. The chemical compositions of the materials are presented in Tables 3 and 4, respectively [33,34].

Table 3. Chemical composition of AL6060.

Element	Fe	Cu	Mn	Mg	Cr	Zn	Ti	Al
% composition	0.10–0.30	≤0.10	≤0.10	0.35–0.6	≤0.05	≤0.15	≤0.10	Rest

Table 4. Chemical composition of M700.

Element	Ti	Nb	V
% composition	0.18	0.10	0.08

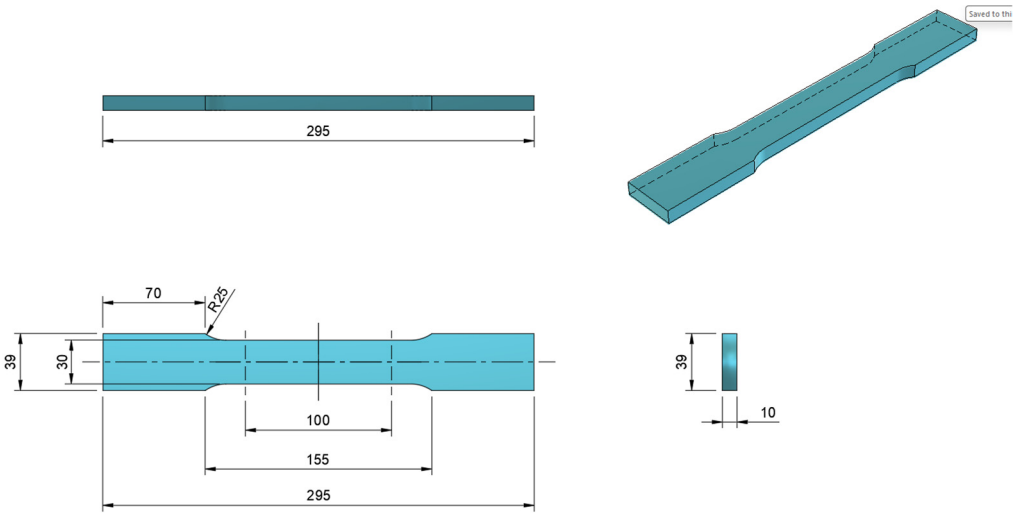

Figure 1. Reference sample dimensions.

3.2. Tension Test Equipment and Methodology

Tensile tests were performed on a QASAR 200 (Figure 2) tensile testing machine from Galdabini S.p.A. (Cardano al Campo, Italy). The load cell capacity of the machine is 200 kN, and the machine is equipped with a motor drive mechanism. A hydraulic-powered wedge-gripping mechanism is implemented in the machine to avoid slippages, where the hydraulic holding force can be increased based on user requirements. The machine was calibrated at the start of the project and, details from the certificate that are relevant to the project are shown below in the respective tables. Table 5 details the uncertainties in the strain measurements for a gauge length of 100 mm. The gauge length measurement had an uncertainty of 100 µm. Table 6 discusses the uncertainties in the load measurement (at different ranges), where the maximum load of the load cell is 200 kN.

Table 5. State of calibration of the extensometer.

l_t [µm]	l_i [µm]	q_b [µm]	Measuring Uncertainty
			Rel [in +/− %]
2000	1985	−15.00	0.18
4000	3972	−28.000	0.17

l_t is the displayed displacement for the calibration standard, l_i is the displayed displacement of the extensometer and q_b is the absolute deviation of the extensometer.

Table 6. State of calibration of the load cell.

F_i [N]	F_1 [N]	F_2 [N]	F_3 [N]	F_{avg} [N]	M_u [±%]
5000	5042	5041.3	5044.3	5042.5	0.12
20,000	20,092	20,023	20,029	20,048	0.24
80,000	79,979	79,936	79,939	79,951	0.12
120,000	119,847	119,714	119,740	119,767	0.12
200,000	199,866	199,822	199,741	199,810	0.12

F_i is the value of the force measuring device of the testing machine, F_1–F_3 is the displayed real force with increasing force, F_{avg} is the average value of the force measurement, and M_u is the relative measuring uncertainty.

Figure 2. QASAR 200 UTM.

The tests were carried out at a constant strain rate of 0.00025 s^{-1}, but it should be noted that the samples were not loaded to failure, since the determination of material properties is beyond the scope of this paper. Instead, the sample was subjected to a three-stage deformation process, where at each stage, the E-value was determined. In the first stage, the sample was loaded with a strain of 0.1%, in the second stage, with a strain of 0.15% and in the last stage, with a strain of 0.2%. In each stage, the sample was loaded at least 25 times and unloaded at each count to check if there were any deviations in the resulting stress–strain curve and to check the modal frequencies at the end of each stage. The process is pictorially shown in Figure 3.

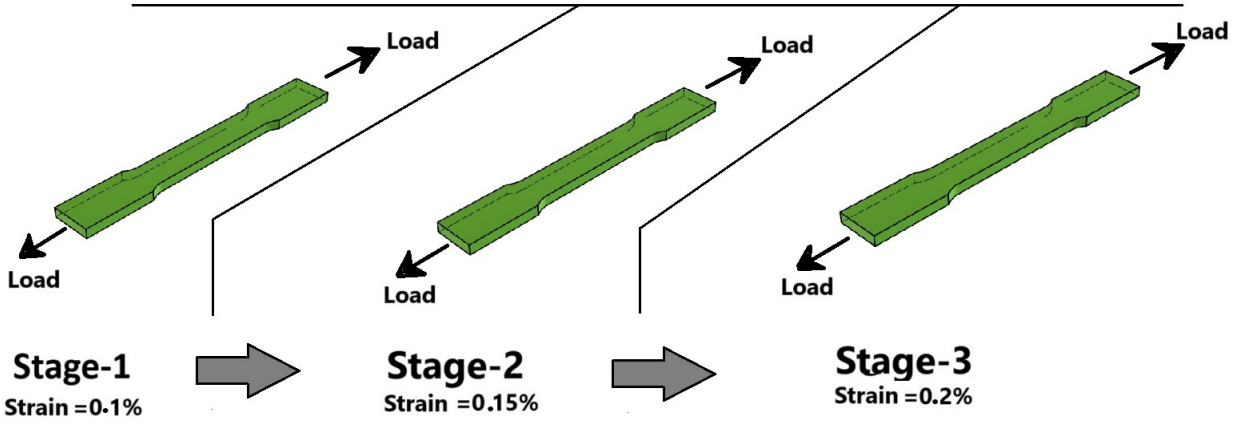

Figure 3. Loading stages of reference samples.

3.3. Acoustic Equipment and Associated Test Methodology

The mechanical excitation of the sample and its subsequent modal vibration depends on the boundary conditions imposed on the sample. The constraints imposed on the sample at its lower end and its excitation are shown in Figure 4. Various methods have been used to mechanically excite the test sample in order to record the sound, but it was observed that simply tapping the sample is sufficient to excite the required modes. To improve

data quality, the sample is excited 10 times at an interval of 5 s. The required mode(s) is identified by simulating it using CAE software and the methodology adopted can be found in [35,36]. The material properties of the samples were determined via tensile tests conducted according to ISO 6892. The properties are as shown in Table 7, and the sample dimensions illustrated in Figure 1 were used for the simulations conducted.

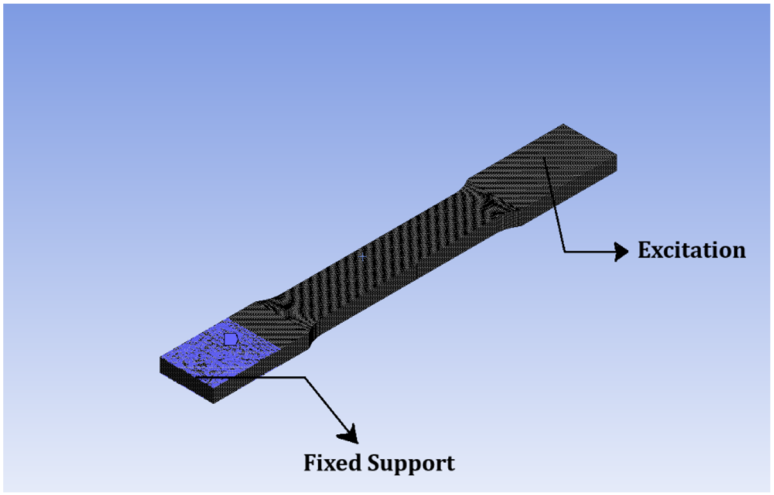

Figure 4. Sample constrained for acoustic excitation.

Table 7. Material properties of the sample material.

Material	Density [kg/m^3]	E-Modulus [GPa]	Poisson's Ratio	Rp0.2 [MPa]	Rm [MPa]
M700	7990	206	0.28	781	800
AL6060	2700	66	0.33	182	211

An ultra-miniature accelerometer (Dytran 3225F, Dytran Instruments Inc., Chatsworth, CA. USA) was used as the sensing element to sense sound signals from the reference sample. The sensor has a frequency range of 2–10 kHz, which has a quartz shear sensing element in a lightweight titanium housing (Figure 5A). Due to advancements in manufacturing technologies, accelerometers featuring low noise and high sensitivity have become ubiquitous. The price of the system is more competitive when compared to high-end acoustic systems used in more critical applications. The data acquisition system consists of a palm-sized USB system, with a sampling rate of 500 S/s to 128 kS/s, thus allowing for high-resolution data capture (see Figure 5B). A suitable adhesion material must be used as a coupling agent between the sensor and the sample, and for this purpose, bee wax was used because of its ease of application, excellent acoustic coupling efficiency, thermal and mechanical stability, and eco-friendliness, making it a superior choice compared to metals or other hard adhesives. Additionally, its low acoustic impedance minimizes reflections at the interface between the sensor and the test sample, effectively reducing signal loss and ensuring optimal coupling of acoustic waves [37].

The structural integration of the sensor system is as shown in the figure below (Figure 6). This involves placing the sensor at the root of the reference sample, below which the reference sample is clamped (similar to the boundary conditions shown in Figure 4). The sound system output is represented as time-domain signals, illustrated in Figure 6, which are subsequently analyzed using fast Fourier transforms to identify the dominant frequencies present in the signal. An algorithm was implemented within the project to convert time-domain to its corresponding frequency-domain. Sampling rate is an important

factor in such conversions and in this case, 16 kHz was adopted (details on the algorithm can be found in [35,36]).

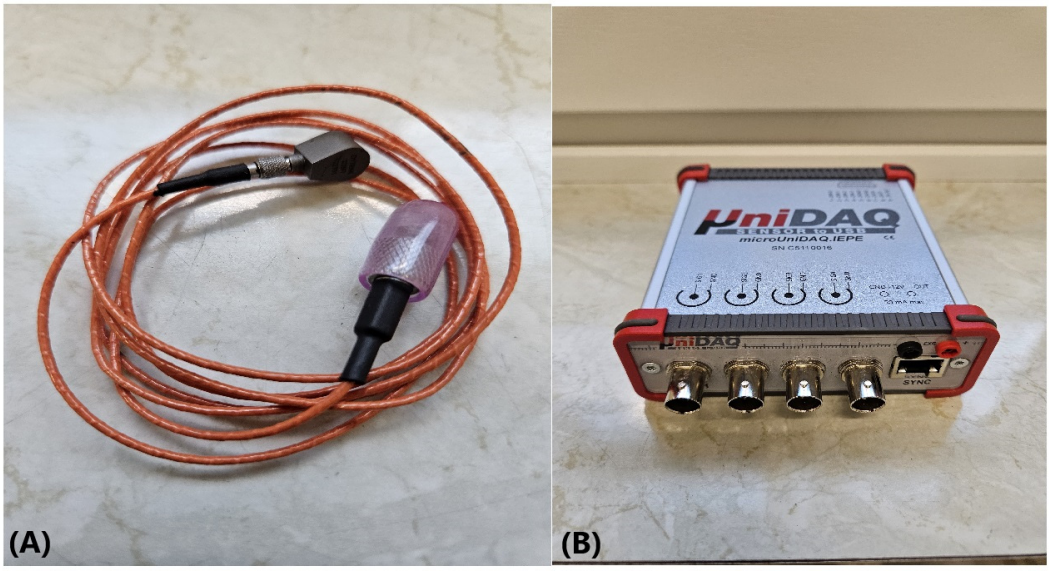

Figure 5. Sound system used in the project: (**A**) Dytran 3225F accelerometer and (**B**) data acquisition system.

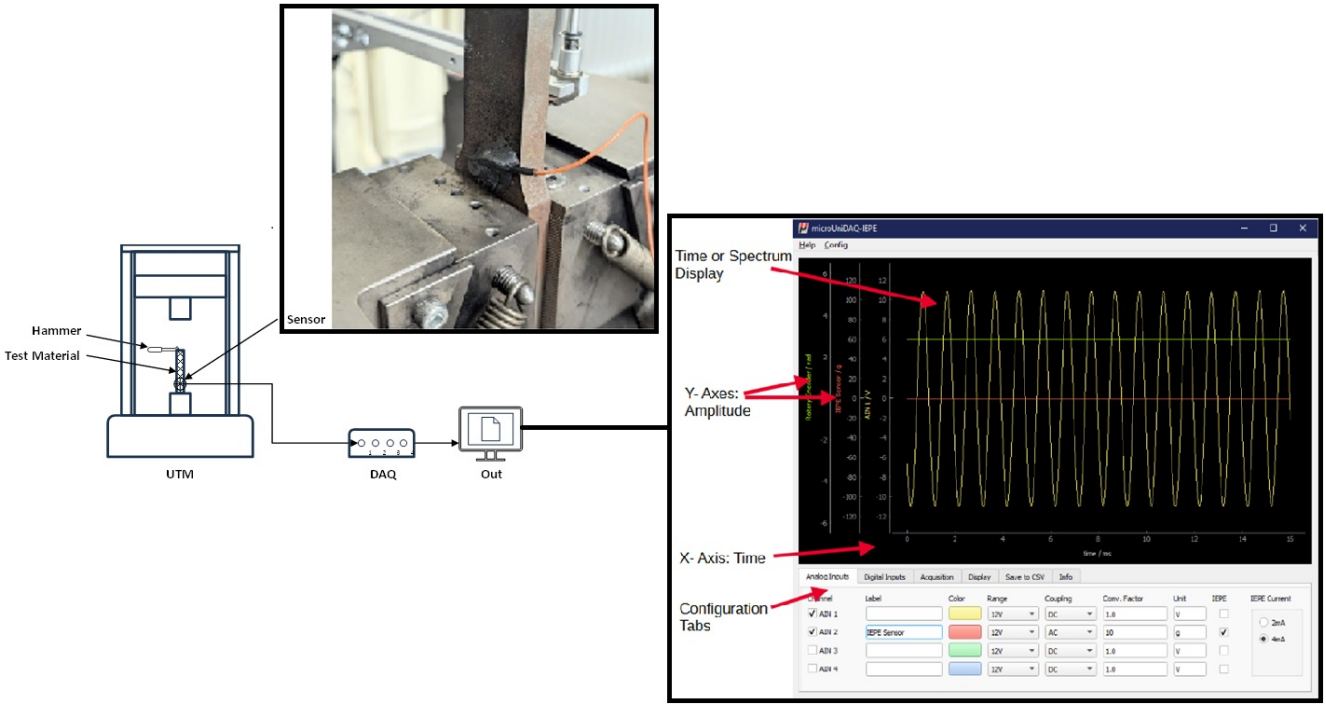

Figure 6. Sensor integration for calibration monitoring.

3.4. Methodology for Developing a Graphical User Interface (GUI) to Keep Track of Calibration of UTMs

The programming language Python (version 3.12.0) is utilized in this research to develop a GUI using the Tkinter [38] library. The architecture used for such a GUI is depicted in Figure 7, in which the GUI represents the final phase of the three-stage process. The first stage involves the UTM and associated sensors for data generation, where the UTM is the Quasar 200 and the accelerometers form the sensorial part. The second stage is subdivided into two parts, where the first part focuses on data acquisition and processing part. This entails raw data acquisition from the UTM including information from the

load cells and the extensometer and the accelerometer for sound signals. The second section includes all the extraction processes, featuring a tailored algorithm that monitors the machine's status. The algorithm is shown in Figure 8 and further details are provided in the following paragraph. The last step is the actual user interface integrated into the system to collect user data to control the test procedure and inform the user about the status of the machine. For this purpose, the Tkinter package of python was used. Tkinter or "Tk interface" is a module of python that provides an interface to the Tk GUI toolkit, developed in TCL (Tool Command Language) and multiplatform, with the support of Linux, MAC OS and MS Windows. Tk is natively present in Linux and MAC, OS and can be easily installed in MS Windows, but it is not part of Python. Widgets, geometry management, and event handling are the three main concepts in Tk, which also apply for Tkinter. Widgets have been used extensively in this project, and these link the algorithm to the user. Since the literature on these concepts is quite exhaustive, readers can find more information in Ref. [38].

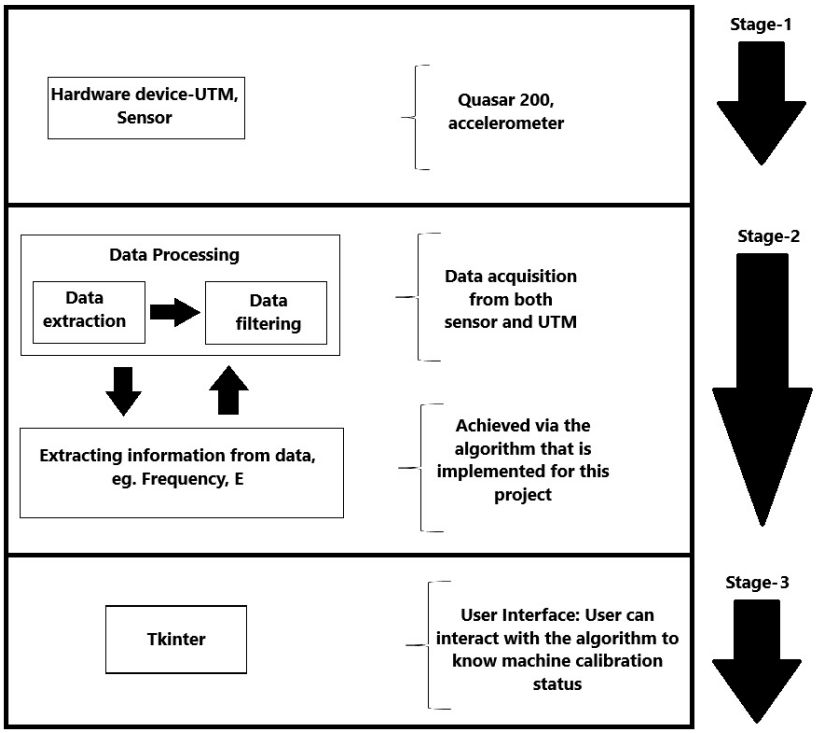

Figure 7. Overview of the system developed for calibration status check.

Based on the overview shown in Figure 7, the basic algorithm for continuously checking the calibration status of the machine is as shown in Figure 8. The algorithm utilizes the data from the "Data processing" module illustrated in Figure 7. From this module, the algorithm has access to both the data from the UTM and the sensor. The former is used to check the machine uncertainties stemming from the load cell and extensometer and the algorithm compares these with the calibration certificate. The latter is used to generate the frequency spectrum to identify the modal frequencies and to calculate the E based on the modes that are flexural in nature. The rest of the modes are omitted by the algorithm, and these include the torsional and extensional nodes if any are seen in the spectrum. These can be identified from the simulated results explained in Section 3.3.

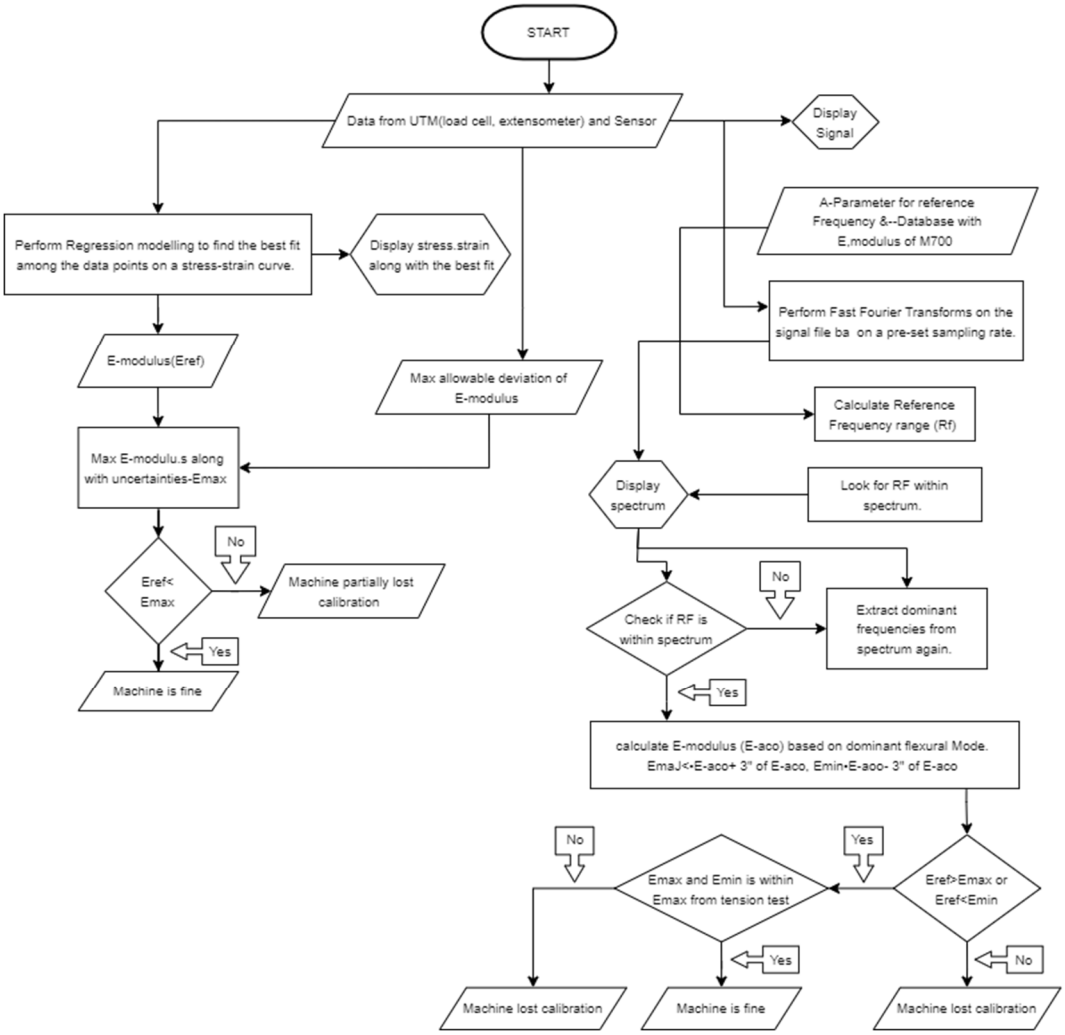

Figure 8. Overview of the algorithm.

4. Results and Discussions

4.1. Comparison of Frequencies from Simulations and Experiments for the Reference Sample

The simulated modal frequencies are displayed in Figure 9 for both the reference sample materials, namely Al6060 and M700. A total of 10 modal frequencies are displayed ranging from a minimum of 130 Hz to 5500 Hz. The distinctive mode shapes are the usual bending (flexural), torsional, and length stretching modes, where deflections are predominant and are symmetric with respect to the mid-planes. The modes are a combination of Mode-1, Mode-2, etc., in an ascending order, and they vary in a mode-specific manner as a function of the mechanical part structures [35,36].

As mentioned earlier in the methodology section, simulations help to identify the frequencies that we want to identify within the frequency spectrum. A frequency spectrum obtained directly from its corresponding time-domain signal contains two or more peaks, which leads to the identification of the wrong modes that one intends to use in the study. An example is shown below, where two peaks are clearly visible. The greater peak of 805 Hz corresponds to the 801 (for Al6060) Hz seen in Figure 9 representing Mode-3, which is a flexural mode. On the other hand, the second peak seen in Figure 10 (1442 Hz) corresponds to Mode-4 (for Al6060), which is also shown in Figure 9. Therefore, since the bending mode frequencies are used to estimate E, simulations are useful tools to identify the required modes, especially in this study. Thus, based on this comparison, the algorithm

under study in this work takes into consideration only the flexural modes and omits the torsional and other un-wanted modes.

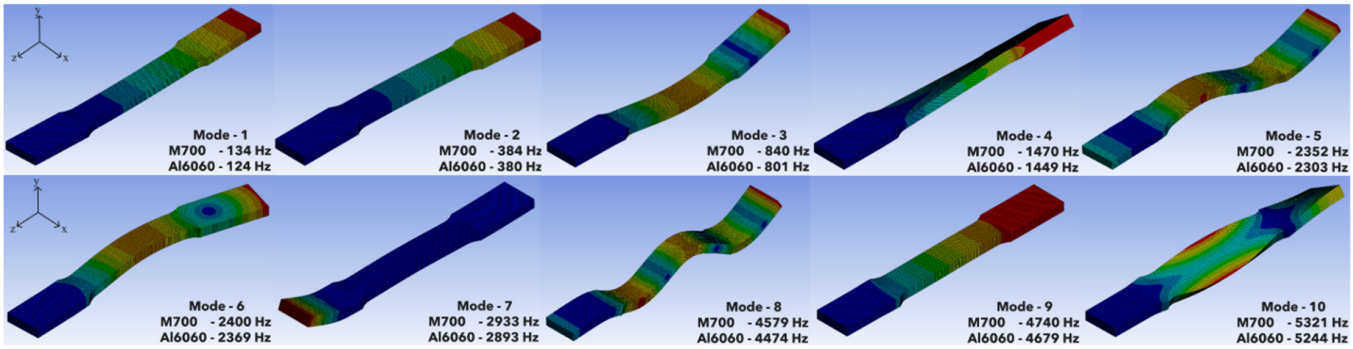

Figure 9. Simulated modal frequencies of the reference sample (both Al6060 and M700).

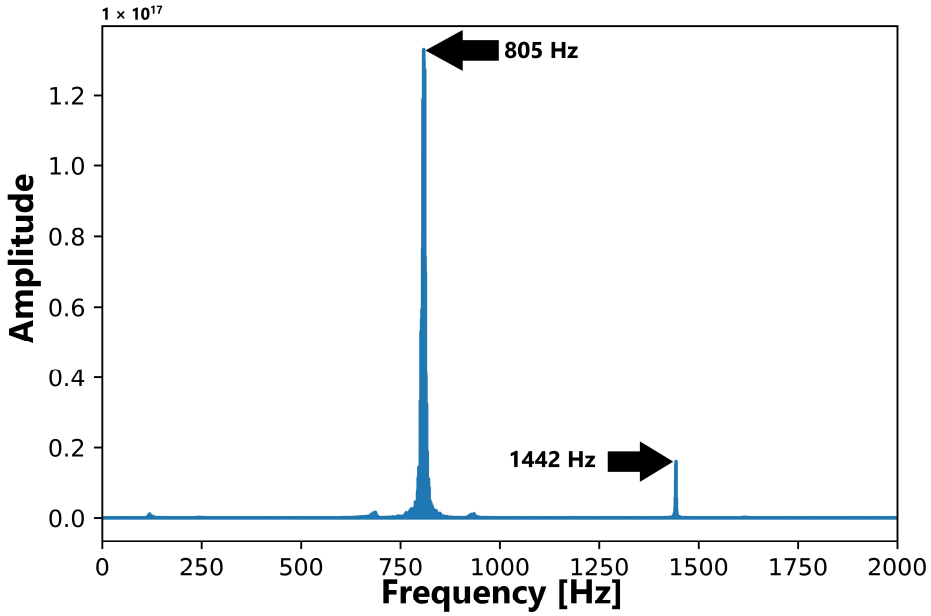

Figure 10. A sample spectrum generated for Al6060.

4.2. Tension Tests and Comparison with Intermittent Frequency Checks

Figure 11 elaborates on the first two stages for Al6060, i.e., 0.1% strain (unloaded after each loading) followed by 0.15% (marked as red in the figure). In both the stages, E was continuously measured, with an average value of 63 GPa in the first stage and 60 GPa in the second stage. In each stage, the sample was loaded and unloaded 25 times; thus, at the end of the third stage, the sample was subjected to cyclic loading 75 times. A 4% decrease in E was noted when transitioning from stage 1 to stage 2. Table 8 further confirms this observation, showing the standard deviations of the first five values, where in both stages, it was less than 1. The frequency spectrum generated after each stage gave the same notable peaks, and this is illustrated in Figure 11C,D. Figure 11C was generated prior to the test while Figure 11D was generated subsequent to the test. Although the frequencies remained the same, the peaks varied, with the first mode (120 Hz) being prominent in Figure 11C, while the third mode is prevalent in Figure 11D, followed by the torsional fourth mode. The appearance of the torsional mode may be linked to the material's low stiffness. This makes it hard to excite the relevant modes without exciting a torsional mode. This is not ideal because once the material is accepted as a reference sample, it will be utilized multiple times to verify the calibration status. This may result in strain hardening causing

the frequencies to shift, in addition to the presence of other modal frequencies. Such a sample would forfeit its reliability as a reference sample and could result in premature or delayed calibration of the UTM. The strain hardening becomes more apparent when the sample is subjected to 0.2% strain, as elaborated in the following paragraph.

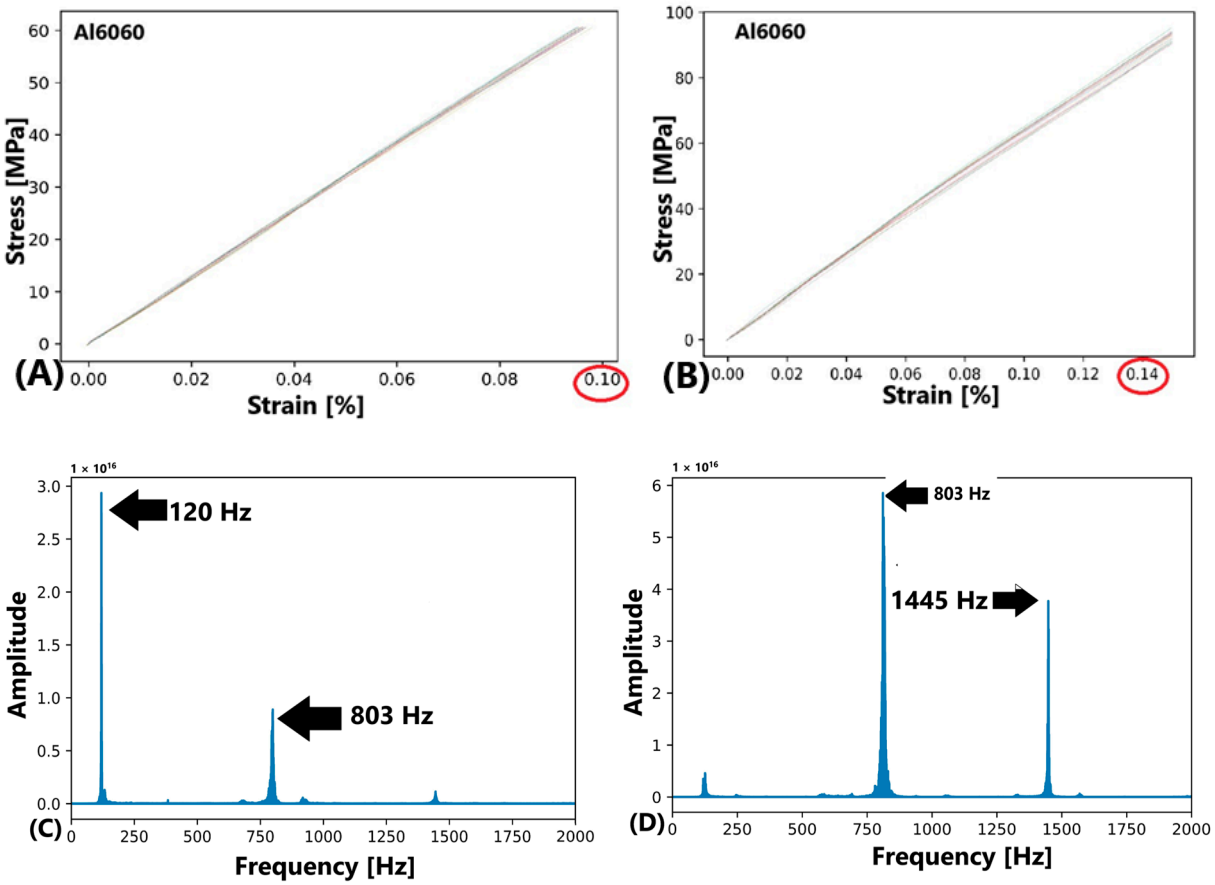

Figure 11. Plots generated for Al6060 from stage 1 to 2. (**A**) Sample loaded until 0.1% strain, (**B**) same sampled loaded subsequently until 0.15% strain, (**C**) spectrum before sample was loaded and (**D**) spectrum after sample was loaded.

Table 8. Young's modulus (E) from stage 1, 2 and 3.

Tests Serial Number	E in Stage 1 [Gpa]	E in Stage 2 [Gpa]	E in Stage 3 [Gpa]
1	64.67	61.04	60.23
2	63.06	61.02	60.74
3	62.13	60.03	61.75
4	62.92	60.19	60.89
5	63.03	60.72	61.81
Standard deviation	0.928	0.468	0.68

Following the previous two stages, the identical sample was subjected to 0.2% strain for 25 repetitions, and the outcomes are displayed in Figure 12A,B. Table 8 presents the first five values of the E obtained in this phase. From Figure 12A, it can be observed that the 25 plots generated for each loading scenario seem very consistent without any observable deviations. The values of E, generated in this case, were the same, and the average value was 61 GPa. The first five values seen in Table 8 have a standard deviation less than 1, thus further confirming these observations. However, the spectra after mechanical excitation

showed a mix of several peaks as illustrated in Figure 12B and this is in contrast to the earlier spectra seen in Figure 11C,D. Although there was a distinct third mode (803 Hz) observed, there were several other peaks (frequencies) that correspond to other modes not considered in this study. Comparable findings were observed in additional samples examined for this research. The appearance of several peaks could be attributed to strain hardening of the material or the early set of fatigue in the material. The continuous loading and unloading at 0.2% strain may have reduced the sample's resistance to fatigue [31]. This supports the earlier findings, meaning that multiple peaks observed in the spectrum are not favourable for a reference sample that will ultimately be utilized to verify the calibration status of the UTMs. Consequently, in the upcoming results, the viability of M700 as a reference sample will be assessed.

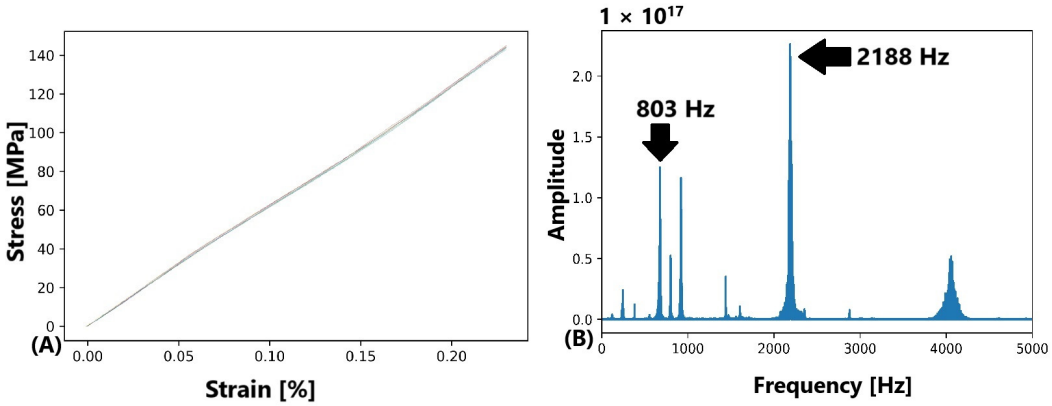

Figure 12. Plots generated for Al6060 during stage 3. (**A**) Sample loaded until 0.2% strain and (**B**) spectrum obtained after test.

Subsequently, the identical methodology was utilized for M700, and the outcomes from the first two stages are displayed in Figure 13A,B, respectively. As in previous instances, after each stage, the samples were assessed for modal frequencies, and it was observed that the sample did not exhibit any change as seen in Figure 13C,D. However, the first two stages of the stress–strain curves showed deviations and when determining E (for each curve), an abrupt change was observed. Table 9 shows the first two stages of five tests each. The variations seen for each test were unsatisfactory, and when the frequency seen in Figure 13C,D was inserted into Equation (10), a value of 202.83 GPa was obtained. Following these observations, the sample was loaded in the third stage.

Following stages 1 and 2, stage 3 was conducted on the same sample and the results are displayed in Figure 14A,B. The observed results differed from those seen in the first two stages. In addition to the curves being consistent, E obtained from each curve had minimum scatter, with the first five presented in Table 10. The mean E from the tensile tests was 204 GPa, whereas the value corresponding to the frequency shown in Figure 14B was 202 GPa, indicating consistency between the two tests. When comparing Figures 12 and 14, i.e., between the performance of Al6060 and M700 in their respective third stages, the spectrums had less clutter in the case of M700. Although the stress–strain plots in both the cases were consistent, the less clutter seen in M700's spectrum is very important. Moreover, M700 has a higher yield limit when compared to Al6060, thus enabling a broader range when applying loads. Furthermore, the fatigue performance of the reference sample is important, as there is a significant influence of yield strength on the fatigue performance of materials [39]. In comparison to the third stage of AL6060 and M700, the less clutter seen here could be attributed to the absence of early-stage fatigue within the material structure, and also the lesser effects of strain hardening. A thorough investigation concentrating on fatigue might provide a better insight in this context. Owing to these observations and

test results, M700 was adopted as the non-destructive reference sample for verifying the calibration status of UTMs.

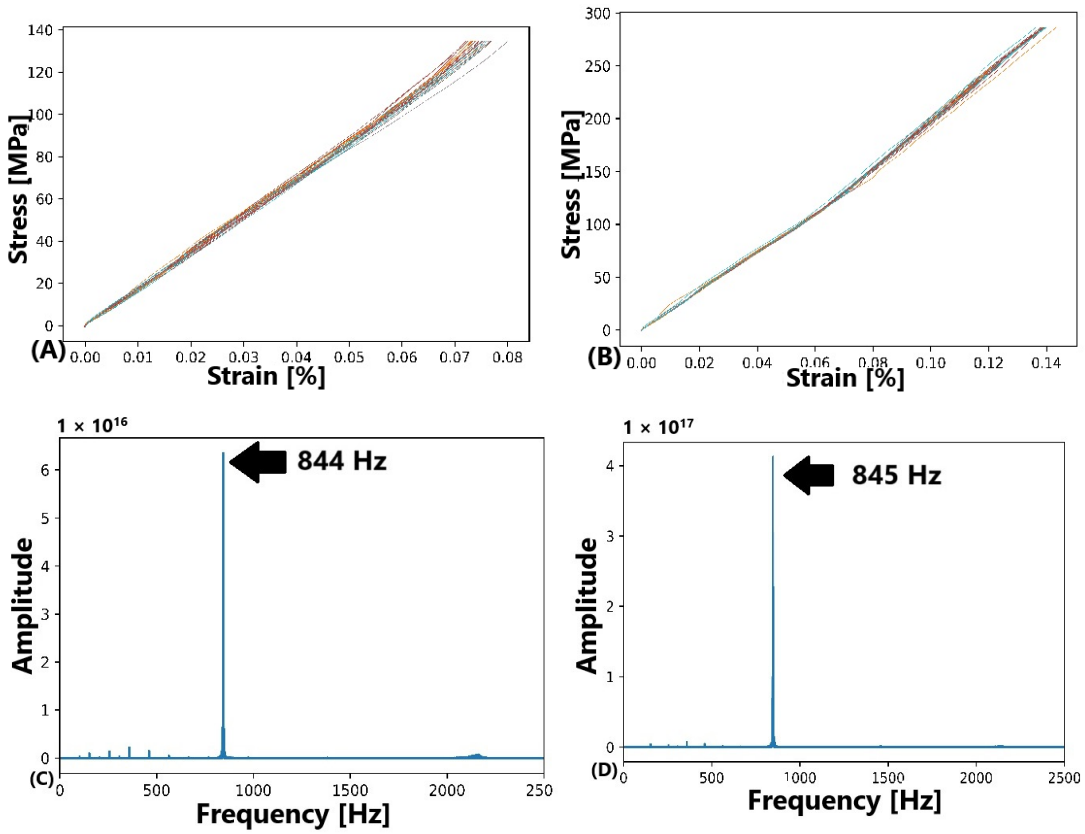

Figure 13. Plots generated for M700 from stage 1 to 2. (**A**) Sample loaded until 0.1% strain, (**B**) Same sampled loaded subsequently until 0.15% strain, (**C**) spectrum before sample was loaded and (**D**) spectrum after sample was loaded.

Table 9. Young's modulus (E) from stage 1 and 2.

Tests Serial Number	E in Stage 1 [Gpa]	E in Stage 2 [Gpa]
1	179.17	212.88
2	209.2	223.06
3	186.35	224.05
4	191.52	223.75
5	214.01	218.92
Standard deviation	4.75	4.75

Table 10. Young's modulus (E) from stage 3.

Tests Serial Number	E in Stage 2 [Gpa]
1	203.97
2	205.54
3	204.08
4	204.06
5	204.84
Standard deviation	0.67

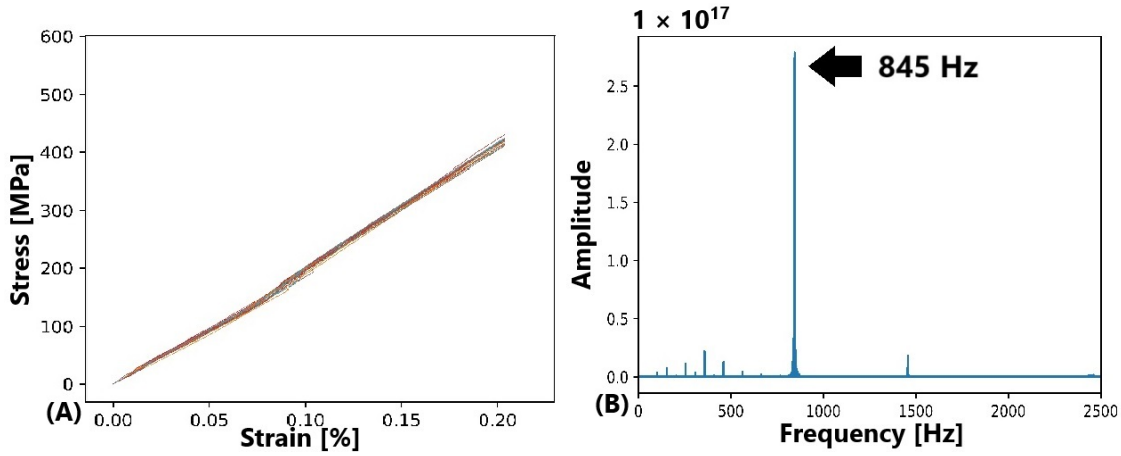

Figure 14. Plots generated for M700 during stage 3. (**A**) Sample loaded until 0.2% strain and (**B**) spectrum obtained after test.

4.3. The Use of GUI to Ascertain Machine Calibration Status

As discussed previously, Tkinter is a module of Python that offers an interface to help interact with the source code to help manage the calibration status of the UTM. Widgets, geometry management and event handling are the three main concepts of Tkinter that assist the user in interacting with the source code. The graphical user interface developed for the project helps the user with the following steps:

1. Processing machine data from tension tests and generating uncertainties outcomes and hence informing the user about the machine status vis-à-vis the extensometer and load cells.
2. Processing data from sound signals and generating outcomes in the form of frequency spectrum and calibration status of the machine based on sound emission analysis carried out by the algorithm.

Some specific operations carried out by the GUI are as follows;

- Generating regression fits based on the linear regression model.
- Ascertaining the co-efficient of regression.
- Checking for uncertainties and deviations from levels mentioned in the calibration certificate.
- Taking in user input with regard to geometric parameters of the reference sample.
- Generating relevant plots such as frequency spectrum.
- Lastly, checking for the calibration status based on the sound signal analysis carried out by the algorithm.

Figure 15A displays a segment of the algorithm, which includes a *def* function that retrieves data from the directory containing pertinent UTM information. Once the *def* function has been plugged into the command of a button widget, pressing it later will input the data for processing. Similarly, the GUI that was generated can be seen in Figure 15B, which highlights the calibration check from the sound signals. The GUI acts as the interface that helps the user interact with the source code shown in Figure 15A.

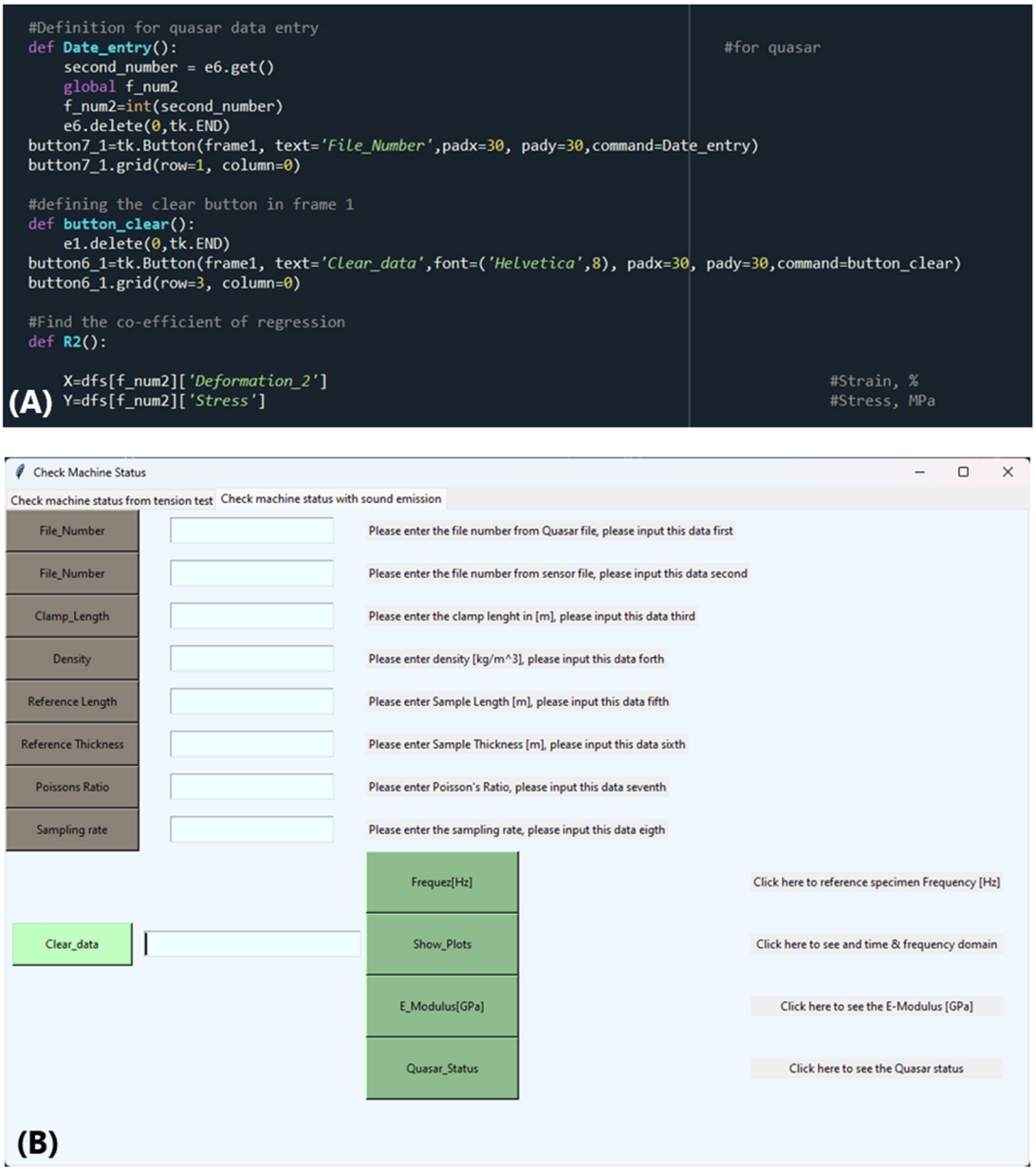

Figure 15. (**A**) Code excerpt from the source code for calibration and (**B**) GUI developed for checking calibration status of machine.

5. Conclusions

The study presents a new method for non-destructive monitoring of UTM calibration using a combination of acoustic techniques and a non-destructive reference sample subjected to tension tests within the elastic region. By combining simulations and experimental analyses, the research identified important modal frequencies in reference samples made from Al6060 and M700 alloys, focusing on flexural modes that are crucial for determining Young's modulus (E). The simulation results, validated through experiments, accurately isolated relevant modal frequencies and excluded non-essential ones such as torsional modes, ensuring that the algorithm precisely tracks the desired flexural frequencies. Tension tests with intermittent frequency checks showed that while Al6060 initially exhibited stability, it experienced significant frequency deviations after repeated loading. This limited its suitability as a reliable reference material for continuous monitoring. In contrast, M700 demonstrated a consistent frequency response, making it a more stable

candidate for long-term calibration tracking. The choice of M700 instead of AL6060 as the reference sample was based on the inconsistencies observed in the frequency spectra following three phases of tension tests, with 25 tests conducted in each phase. Consequently, following the third phase, either as a result of strain hardening or an early manifestation of fatigue in the structure, AL6060 displayed multiple peaks in the spectra when subjected to mechanical excitation.

The algorithm developed is integrated with a GUI, making it a robust tool for real-time calibration assessment. With the GUI, users can input geometric parameters, conduct regression analysis, and evaluate machine performance based on sound emission data. It systematically processes information from both tension tests and acoustic signals, providing a comprehensive assessment of UTM calibration status by comparing observed frequencies with those predicted by simulations.

The validation of the proposed system has shown that the geometric constraints (clamping at the root of the sample) imposed on the sample have a significant impact on the algorithm output. Precise measurement of the clamp length and its relation to the total sample length is therefore very important. This emphasizes the importance of precise input values to guarantee accurate results. Even with continuous use, the reference sample (M700) has maintained its elastic properties, making it a dependable tool for ongoing calibration monitoring. This approach minimizes the need for traditional, often disruptive, calibration processes by offering a continuous, real-time assessment mechanism. As a result, it reduces machine downtime and improves operational efficiency.

The results show that combining acoustic monitoring methods with calibration protocols has the potential to provide a reliable solution for maintaining the accuracy and dependability of UTMs. This innovation can be especially useful in industrial settings where machine precision is crucial. Future research could concentrate on broadening the algorithm's scope to cover a wider variety of materials and testing conditions, as well as improving the acoustic monitoring methods to increase sensitivity and accuracy. These developments would further establish this approach as a valuable tool in the field of machine calibration and quality assurance.

Author Contributions: S.P.S.: Conceptualization; writing—original draft; methodology; formal analysis; validation; visualization; writing—review and editing; data curation. R.S.: Investigation; validation; software; data curation; writing—original draft; formal analysis; visualization; writing—review A.H.: Software; writing—original draft. E.M.: Project administration; data curation. S.S.: Conceptualization; funding acquisition; methodology; project administration; writing—review and editing; resources; supervision; validation. All authors have read and agreed to the published version of the manuscript.

Funding: This research was funded by the Federal Ministry for Economic Affairs and Climate Action (Germany), under the grant number KK5410401KP1 (https://www.haw-hamburg.de/forschung/forschungsprojekte-detail/project/project/show/reusedetect/).

Institutional Review Board Statement: Not applicable.

Informed Consent Statement: Not applicable.

Data Availability Statement: Available on demand.

Acknowledgments: This is a part of the research project "ReUseDetect" along with cooperation partner SCHÜTZ + LICHT Prüftechnik GmbH. Luca Zenone, Area Manager, SCHÜTZ + LICHT Prüftechnik GmbH.

Conflicts of Interest: The authors declare no conflicts of interest.

References

1. Lord, J.; Rides, M.; Loveday, M. *'Tenstand' WP3 Final Report: Modulus Measurement Methods*; DEPC-MPE 016; NPL Report; NFL: New York, NY, USA, 2018.
2. Loveday, M.S. Towards a tensile reference material. In *Harmonisation of Testing Practise for High Temperature Materials*; Loveday, M.S., Gibbons, T.B., Eds.; Springer: Dordrecht, The Netherlands, 1992. [CrossRef]
3. *ISO 9001*; Quality Management Systems—Requirements. The International Organization for Standarization: Geneva, Switzerland, 2015.
4. *EN 10001-1*; Metallic Materials-Tensile Testing-Part 1: Method of Test at Ambient Temperature. European Committee for Standardization: Brussels, Belgium, 2001.
5. *ASTM E8*; Standard Test Methods for Tension Testing of Metallic Materials. ASTM International: West Conshohocken, PA, USA, 2024.
6. *ISO 6892-1:2019*; International Standard for Metallic Materials-Tensile Testing at Ambient Temperature. ISO: Geneva, Switzerland, 2019.
7. *ISO 9513:2012*; Metallic Materials-Calibration of Extensometer Systems Used in Uniaxial Testing. The International Organization for Standarization: Geneva, Switzerland, 2012.
8. Sebastian, S.; Marion, M. A new approach for the determination of the linear elastic modulus from uniaxial tensile tests of sheet metals. *J. Mater. Process. Technol.* **2017**, *241*, 64–72.
9. Kostic, S.; Miljojkovic, J.; Simunovic, G.; Vukelic, D.; Tadic, B. Uncertainty in the determination of elastic modulus by tensile testing. *Eng. Sci. Technol. Int. J.* **2022**, *25*, 100998. [CrossRef]
10. Sebastián, T.; Walter, S.; Alberto, S.; Angel, M. Measurement of the Young's modulus in particulate epoxy composites using the impulse excitation technique. *Mater. Sci. Eng. A* **2010**, *527*, 4619–4623.
11. Lord, J.D.; Morrell, R.M. *Elastic Modulus Measurement, Good Practice Guide No. 98*; National Laboratory: Teddington, UK, 2006.
12. Ho, H.C.; Chung, K.F.; Huang, M.X.; Nethercot, D.A.; Liu, X.; Jin, H.; Wang, G.D.; Tian, Z.H. Mechanical properties of high strength S690 steel welded sections through tensile tests on heat-treated coupons. *J. Constr. Steel Res.* **2020**, *166*, 105922. [CrossRef]
13. Viala, R.; Placet, V.; Cogan, S. Identification of the anisotropic elastic and damping properties of complex shape composite parts using an inverse method based on finite element model updating and 3D velocity fields measurements (FEMU-3DFV): Application to bio-based composite violin soundboards. *Compos. Part A Appl. Sci. Manuf.* **2018**, *106*, 91–103. [CrossRef]
14. *EN 843-2:2006*; Advanced Technical Ceramics-Mechanical Properties of Monolithic Ceramics at Room Temperature-Part 2:Determination of Young's Modulus, Shear Modulus and Poisson's Ratio. German Version; Beuth Publishing DIN: Berlin, Germany, 2007.
15. Roebben, G.; Bollen, B.; Brebels, A.; van Humbeeck, J.; van der Biest, O. Impulse excitation apparatus to measure resonant frequencies, elastic moduli, and internal friction at room and high temperature. *Rev. Sci. Instrum.* **1997**, *68*, 4511–4515. [CrossRef]
16. Trubitz, P.; Rehmer, B.; Pusch, G. Tagung wekstoffprüffung. In *Die Ermittlung Elastischer Konstanten Von Gusseisenwerkstoffen*; Werkstoff-Informationsges: Neu-Ulm, Germany, 2004; pp. 267–272.
17. Antunes, J.M.; Fernandes, J.V.; Sakharova, N.A.; Oliveira, M.C.; Menezes, L.F. On the determination of the Young's modulus of thin films using indentation test. *Int. J. Solids Struct.* **2007**, *44*, 8313–8334. [CrossRef]
18. Rossin, J.; Goodlet, B.; Torbet, C.; Musinski, W.; Cox, M.; Miller, J.; Groeber, M.; Mayes, A.; Biedermann, E.; Smith, S.; et al. Assessment of grain structure evolution with resonant ultrasound spectroscopy in additively manufactured nickel alloys. *Mater. Charact.* **2020**, *167*, 110501. [CrossRef]
19. Gabauer, W. *The Determination of Uncertainties in Tensile Testing, UNCERT Manual of Codes of Practice for the Determination of Uncertainties in Mechanical Tests on Metallic Materials*; Code of Practice No. 07; VOEST-ALPINE STAHL LINZ GmbH: Linz, Austria, 2000.
20. Moffat, R.J. Describing the uncertainties in experimental results. *Exp. Therm. Fluid Sci.* **1988**, *1*, 3–17. [CrossRef]
21. Holman, J.P. *Experimental Methods for Engineers*, 8th ed.; McGraw-Hill series in mechanical engineering; McGraw-Hill: New York, NY, USA, 2011.
22. BIPM; IEC; IFCC; ISO; IUPAC; IUPAP; OIML. *Guide to the Expression of Uncertainty in Measurement*; Geneva First Edition; International Organization for Standardization: Geneva, Switzerland, 1993; ISBN 92-67-10188-9.
23. Bell, S. A beginner's guide to uncertainty of measurement. In *Measurement Good Practise Guide*; No 11; NPL: Teddington, UK, 1999.
24. Kłysz, S.; Lisiecki, J. Selected problems of measurement uncertainty-Part 2. *Tech. Sci.* **2008**, *11*, 265–276.
25. Lord, J.D.; Morrell, R.M. Elastic modulus measurement-obtaining reliable data from the tensile test. *Metrologia* **2010**, *47*, 41–49. [CrossRef]
26. Barboni, L.; Gillich, G.R.; Chioncel, C.P.; Hamat, C.O.; Mituletu, I.C. A method to precise determine the Young's modulus from dynamic measurements. *IOP Conf. Ser. Mater. Sci. Eng.* **2018**, *416*, 012063. [CrossRef]
27. Hockauf, K.; Wagner, M.F.X.; Halle, T.; Niendorf, T.; Hockauf, M.; Lampke, T. Influence of precipitates on low-cycle fatigue and crack growth behavior in an ultrafine-grained aluminum alloy. *Acta Mater.* **2014**, *80*, 250–263. [CrossRef]
28. Hockauf, K.; Halle, T.; Hockauf, M.; Wagner, M.F.X.; Lampke, T. Near-threshold fatigue crack propagation in an ECAP-processed ultrafine-grained aluminium alloy. *Mater. Sci. Forum* **2010**, *667*, 873–878. [CrossRef]
29. Bray, G.H.; Glazov, M.; Rioja, R.J.; Li, D.; Gangloff, R.P. Effect of artificial aging on the fatigue crack propagation resistance of 2000 series aluminum alloys. *Int. J. Fatigue* **2001**, *23*, 265–276. [CrossRef]

30. Andersen, S.J.; Zandbergen, H.W.; Jansen, J.; TrÆholt, C.; Tundal, U.; Reiso, O. The crystal structure of the β′′ phase in Al–Mg–Si alloys. *Acta Mater.* **1998**, *46*, 3283–3298. [CrossRef]
31. Rymer, L.M.; Winter, L.; Hockauf, K.; Lampke, T. Artificial aging time influencing the crack propagation behavior of the aluminium alloy 6060 processed by equal channel angular pressing. *Mater. Sci. Eng. A* **2021**, *811*, 141039. [CrossRef]
32. *DIN 50125*; Prüfung Metallischer Werkstoffe-Zugproben (Testing of Metallic Materials-Tensile Tests Pieces). Deutsches Institut für Normung: Berlin, Germany, 2022.
33. Vieth, P.; Borgert, T.; Homberg, W.; Grundmeier, G. Assessment of mechanical and optical properties of Al 6060 alloy particles by removal of contaminants. *Adv. Eng. Mater.* **2023**, *25*, 2201081. [CrossRef]
34. Klein, M.; Spindler, H.; Luger, A.; Rauch, R.; Stiaszny, P.; Eigelsberger, M. Thermomechanically hot rolled high and ultra high strength steel grades-processing, properties and applications. *Mater. Sci. Forum* **2005**, *500–501*, 543–550. [CrossRef]
35. Alaparthi, S.; Subadra, S.P.; Sheikhi, S. A smart, data-driven approach to qualify additively manufactured steel samples for print-parameter-based imperfection. *Materials* **2024**, *17*, 2513. [CrossRef]
36. Alaparthi, S.; Subadra, S.P.; Skaria, R.; Mayer, E.; Sheikhi, S. A study on the effect of print parameters on the internal structural quality of 316L samples via laser powder bed fusion: Experimental and algorithmic approach. *Eng. Rep.* **2024**, *6*, e12996. [CrossRef]
37. Ozmen, G.C.; Safaei, M.; Lan, L.; Inan, O.T. A novel accelerometer mounting method for sensing performance improvement in acoustic measurements from the knee. *J. Vib. Acoust.* **2021**, *143*, 031006. [CrossRef]
38. Beniz, D.B.; Espindola, A.M. Using Tkinter of python to create graphical user interface (GUI) fir scripts in LNLS. In Proceedings of the Proceedings if PCaPAC2016, Campinas, Brazil, 25–28 October 2016.
39. Leitner, M.; Barsoum, Z. Effect of increased yield strength, R-ratio, and plate thickness on the fatigue resistance of high-frequency mechanical impact (HFMI)-treated steel joints. *Weld. World* **2020**, *64*, 1245–1259. [CrossRef]